

Correlated Electron Effects in Chromium Trihalide Heterostructures with Graphene: A Tight-Binding Model Perspective

Igor Rozhansky and Vladimir Fal'ko

National Graphene Institute, University of Manchester, Manchester M13 9PL, United Kingdom

(Dated: April 30, 2024)

In this study, we present an effective tight-binding model for an accurate description of the lowest energy quadruplet of conduction band in a ferromagnetic CrX_3 monolayer, tuned to the complementary *ab initio* density functional theory simulations. This model, based on a minimum number of chromium orbitals, captures a distinctively flat dispersion in those bands but requires taking into account hoppings beyond nearest neighbours, revealing ligand-mediated electron pathways connecting remote chromium sites. Doping of states in the lowest conduction band of CrX_3 requires charge transfer, which, according to recent studies [1–3], can occur in graphene(G)/ CrX_3 heterostructures. Here, we use the detailed description of the lowest conduction band in CrI_3 to show that G/ CrI_3 /G and G/ CrI_3 are type-II heterostructures where light holes in graphene would coexist with heavy electrons in the magnetic layer, where the latter can be characterised by Wigner parameter $r_s \sim 15 - 20$ (as estimated for hBN-encapsulated structures).

I. INTRODUCTION

Chromium trihalides (CrX_3 , where $X = \text{Cl}, \text{Br}, \text{or I}$) form a fascinating family of van der Waals materials, celebrated for their versatile magnetic properties [4–12]. Over the recent years a broad range of studies of these magnetic insulators has been performed on both bulk materials and atomically thin films produced by mechanical exfoliation [1, 13–26]. While the main focus of those studies was on magnetic properties of CrX_3 compounds and their dependence on the number of layers [13, 27–33], various CrX_3 films were also implemented in heterostructures with other two-dimensional (2D) materials, like graphene, with a view to proximitise ferromagnetic exchange [2, 3, 34, 35]. A by-product of such studies was an observation of a substantial charge transfer between graphene and CrX_3 reported by several groups [1, 2], attributed to electrons filling narrow conduction bands of CrX_3 [18, 20], rather than impurity states inside its bandgap.

The above-mentioned observation opens an interesting avenue towards creating a 2D material that would combine both highly mobile holes in graphene with strongly-correlated heavy electrons in CrX_3 . Such a system is sketched in Fig. 1: a trilayer assembled from two graphenes with an embedded CrX_3 monolayer, where the transfer of electrons is hosted by the lowest spin-polarised conduction band of CrX_3 . To describe this band (together with three more bands that belong to a quadruplet traced [18, 20, 27, 36–39] to d-orbitals of chromium), we develop an effective tight-binding (TB) model based on a minimal number of Cr orbitals and parametrised by comparison with density-functional theory (DFT) calculations for CrI_3 . This gives us an access to the accurate description of the conduction band edge across the entire Brillouin zone, hence, obtaining a description of doping features of G/ CrI_3 /G stacks, and a possibility to estimate the Wigner parameter for the heavy electrons.

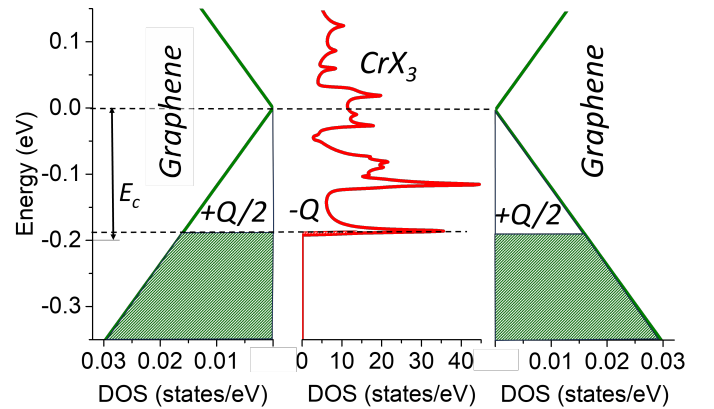


FIG. 1. **Charge transfer in G/ CrX_3 /G trilayer.** The density of states for graphene (left and right) and CrX_3 (center) is shown with an offset E_c ($E_c = 0.2$ eV for CrI_3 as in Ref. [40]), which leads to the transfer of electrons from graphene to the lowest empty band of the d-orbitals-based quadruplet in CrX_3 highlighted in Fig. 2. Painted areas indicate occupied states.

II. TIGHT-BINDING MODEL FOR CRX_3 MONOLAYER

In the crystal structure [41–44] of CrX_3 , illustrated in Fig. 2a, metal ions form a honeycomb middle-sublayer lattice, bonded by halogen atoms in the outer sublayers. Following an analogy with graphene, we divide Cr sites into A and B sublattices. Similarly, to graphene, the crystal lattice has inversion symmetry with respect to the centres of the honeycombs and $y \rightarrow -y$ mirror symmetry; however, it lacks mirror symmetry with respect to the horizontal plane and $x \rightarrow -x$ mirror symmetry, due to three out of six nearest halogens atoms lifted into the top sublayer and the other three pushed down to the bottom sublayers. This makes the symmetry group of the crystal $D3d$.

Recent *ab initio* DFT modelling of various CrX_3 mono-

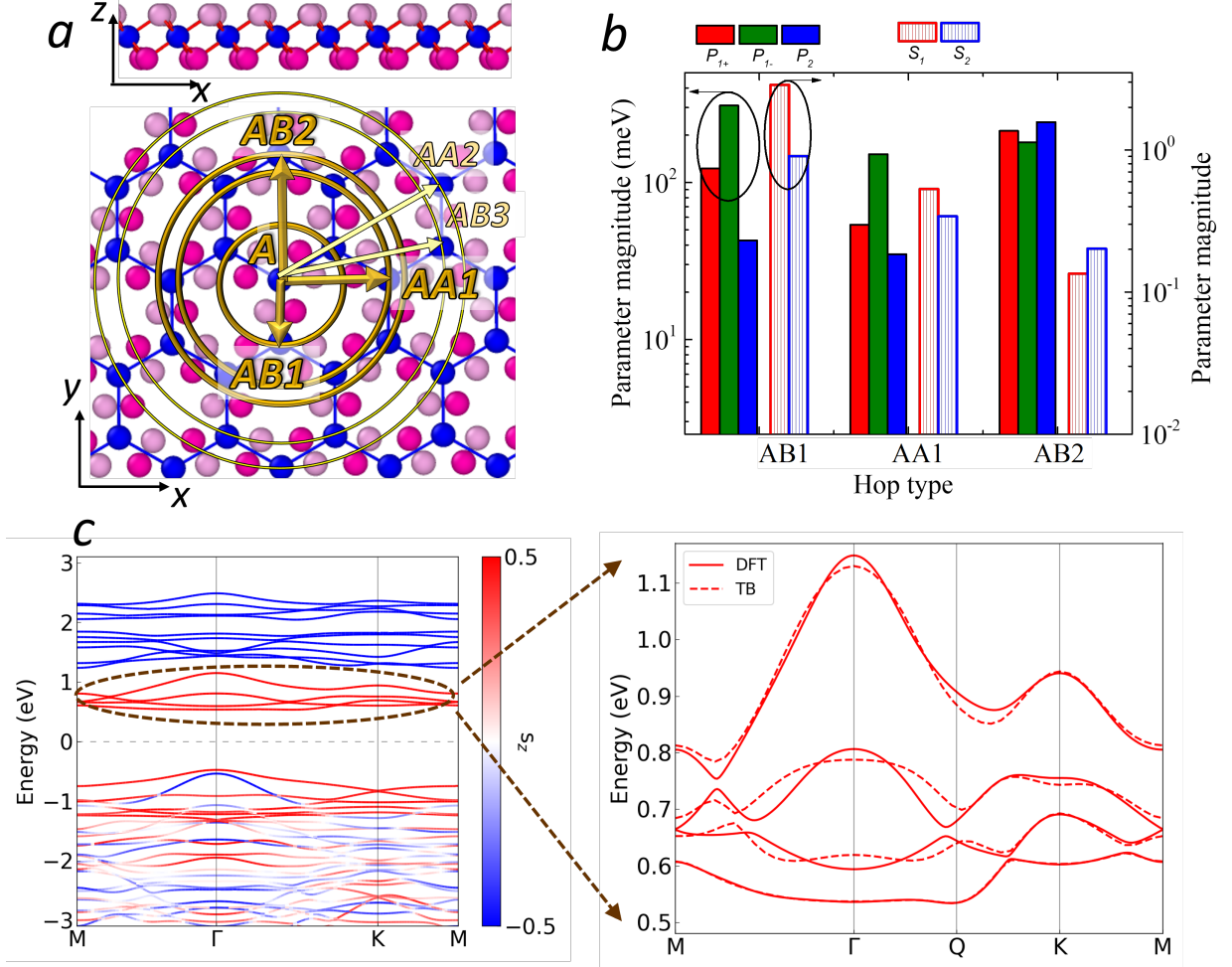


FIG. 2. **Parametrisation of the tight-binding model of CrI_3 using its DFT-computed band structure.** (a) Lattice structure of CrX_3 monolayers ($X=\text{I,Cl,Br}$). Cr ions (blue circles) form a honeycomb lattice; lighter and darker pink circles show halogen positions in upper and lower sublayers. Yellow lines show coordination circles labelled with a hop type. (b) The magnitudes of parameters used in the parametrisation. (c) Left: DFT-calculated band structure of CrI_3 (with SOC taken into account) with colour-coding reflecting spin polarisation of the bands. The bottom of conduction band is dominated by a quadruplet formed of chromium orbitals in Eq. 1 implemented in the tight-binding model (3). Right: the result of tight-binding model (3) parametrisation (Table I), which accounts for Cr-Cr hoppings up to 3rd neighbour, compared with the DFT data.

layers has indicated that wavefunctions of a quadruplet of the lowest spin-polarized conduction bands are dominated by d-orbitals of chromium atoms [18, 20, 27, 36–39]. Therefore, in the TB model described below, we implement a basis of mixed orbitals that would belong to $e_{g\sigma}$ doublet at each Cr site, where, in addition to d-orbitals we include a permitted admixture of p-orbitals as a way to mimic the hybridisation with halogen atoms:

$$\begin{aligned}
 \psi_{A1} &= \alpha Y_2^2 - \beta (\zeta Y_2^{-1} + \eta Y_1^{-1}); \\
 \psi_{A2} &= \alpha Y_2^{-2} + \beta (\zeta Y_2^1 - \eta Y_1^1); \\
 \psi_{B1} &= \alpha Y_2^2 - \beta (\zeta Y_2^{-1} - \eta Y_1^{-1}); \\
 \psi_{B2} &= \alpha Y_2^{-2} + \beta (\zeta Y_2^1 + \eta Y_1^1); \\
 \alpha^2 + \beta^2 &= 1; \quad \zeta^2 + \eta^2 = 1.
 \end{aligned} \tag{1}$$

Here, Y_l^m are spherical harmonics; α, β are on-site mixing parameters for $m = 2(-2)$ and $m = -1(1)$ angular harmonics; ζ, η describe the mixing between $l = 1$ and $l = 2$ harmonics with $|m| = 1$; ψ_{Aj} and ψ_{Bj} are associated with two orbitals ($j = 1, 2$) at A and B sites, respectively. The spatial distribution of the density of such basis states reflects the 3-fold rotational symmetry of the CrX_3 lattice. This basis gives $E \times E$ reducible representation of the $D3d$ point group.

We use this basis as a minimal set to formulate an effective TB model describing the conduction band quadruplet highlighted in the CrI_3 monolayer band-structure displayed in Fig. 2b. This band structure was obtained by DFT modelling of the ferromagnetic CrI_3 monolayer (magnetized along z -axis) using the DFT+ U + J scheme within the Quantum-Espresso *ab initio* pack-

age [45, 46] with fully relativistic pseudopotentials (thus, taking the full account of spin-orbit coupling (SOC)) and the Perdew-Burke-Ernzerhof (PBE) approximation for the exchange-correlation functional [47]. For U and J , we take $U = 1.5$ eV and $J = 0.5$ eV [21].

For the plane-wave version of the TB model we use

Bloch functions and effective Schrodinger equation,

$$\begin{aligned}\chi_{A_j, \mathbf{q}}(\mathbf{r}) &= \sum_{\mathbf{R}} \frac{e^{i\mathbf{q}\mathbf{R}}}{\sqrt{N}} \psi_{A_j}(\mathbf{r} - \mathbf{R}); \\ \chi_{B_j, \mathbf{q}}(\mathbf{r}) &= \sum_{\mathbf{R}} \frac{e^{i\mathbf{q}\mathbf{R}}}{\sqrt{N}} \psi_{B_j}(\mathbf{r} - \mathbf{R}); \\ (\mathcal{H}_{\mathbf{q}} - E_{\mathbf{k}} \mathcal{S}_{\mathbf{q}}) \begin{pmatrix} A_1 \\ A_2 \\ B_1 \\ B_2 \end{pmatrix}_k &= 0, \end{aligned} \quad (2)$$

where \mathbf{R} are vectors of dimensionless Bravais lattice with a unit period, $\mathbf{q} = \mathbf{k}a_0$ is dimensionless wavevector (normalised by lattice constant a_0 , \mathbf{k} is the wavevector), and $\mathcal{H}_{\mathbf{q}}$ and $\mathcal{S}_{\mathbf{q}}$ are the TB Hamiltonian and overlap matrix. We formally describe the structure of \mathcal{S} and \mathcal{H} using Slater-Koster approach as follows:

$$\begin{aligned}\mathcal{H}_{\mathbf{q}} &= \sum_{i,j} \left((-1)^{(j-1)} \varepsilon_s \delta_{ij} + t_{ij}^{(2)} \right) (a_i^+ a_j + b_i^+ b_j) + \sum_{i,j}^{\lambda=1,3} t_{ij}^{(\lambda)} a_i^+ b_j + H.c.; \\ \mathcal{S}_{\mathbf{q}} &= \sum_{i,j} \left(\delta_{ij} + s_{ij}^{(2)} \right) (a_i^+ a_i + b_i^+ b_i) + \sum_{i,j}^{\lambda=1,3} s_{ij}^{(\lambda)} a_i^+ b_j + H.c.; \\ s_{11}^{(\lambda)} &= s_{22}^{(\lambda)} = f_1^{(\lambda)} S_1^{(\lambda)}; \quad s_{12}^{(\lambda=1,3)} = f_2^{(\lambda)} S_2^{(\lambda)}; \quad s_{21}^{(\lambda=1,3)} = f_3^{(\lambda)} S_2^{(\lambda)}; \quad s_{12}^{(2)} = s_{21}^{(2)*} = f_2^{(2)} S_2^{(2)}; \\ t_{11}^{(\lambda)} &= f_1^{(\lambda)} P_{1+}^{(\lambda)}; \quad t_{22}^{(\lambda)} = f_1^{(\lambda)} P_{1-}^{(\lambda)}; \quad t_{12}^{(\lambda=1,3)} = f_2^{(\lambda)} P_2^{(\lambda)}; \quad t_{21}^{(\lambda=1,3)} = f_3^{(\lambda)} P_2^{(\lambda)}; \quad t_{12}^{(2)} = t_{21}^{(2)*} = f_2^{(2)} P_2^{(2)}; \\ S_{n=1,2}^{(\lambda)} &= \alpha^2 \left(3S_{dd\sigma}^{(\lambda)} + 4S_{dd\pi}^{(\lambda)} + S_{dd\delta}^{(\lambda)} \right) - 4\beta^2 \left[(-1)^{\lambda \cdot (n-1)} \zeta^2 \left(S_{dd\delta}^{(\lambda)} - (-1)^n S_{dd\pi}^{(\lambda)} \right) + (-1)^{\lambda \cdot n} \eta^2 \left(S_{pp\sigma}^{(\lambda)} - (-1)^n S_{pp\pi}^{(\lambda)} \right) \right]; \\ P_{1\pm}^{(\lambda)} &= \sum_{s=0,1} (\pm 2)^s \alpha^2 \left(3V_{dd\sigma}^{(s,\lambda)} + 4V_{dd\pi}^{(s,\lambda)} + V_{dd\delta}^{(s,\lambda)} \right) + 4(\mp 1)^s \beta^2 \left[\zeta^2 \left(V_{dd\delta}^{(s,\lambda)} + V_{dd\pi}^{(s,\lambda)} \right) + (-1)^\lambda \eta^2 \left(V_{pp\sigma}^{(s,\lambda)} + V_{pp\pi}^{(s,\lambda)} \right) \right]; \\ P_2^{(\lambda)} &= \alpha^2 \left(3V_{dd\sigma}^{(0,\lambda)} - 4V_{dd\pi}^{(0,\lambda)} + V_{dd\delta}^{(0,\lambda)} \right) - 4\beta^2 \left[(-1)^\lambda \zeta^2 \left(V_{dd\delta}^{(0,\lambda)} - V_{dd\pi}^{(0,\lambda)} \right) + \eta^2 \left(V_{pp\sigma}^{(0,\lambda)} - V_{pp\pi}^{(0,\lambda)} \right) \right]; \\ f_n^{(1)} &= \frac{e^{-iq_y}}{4} \left[e^{\frac{3iq_y}{2}} \cos \left(\frac{\sqrt{3}q_x}{2} - \frac{2\pi(n-1)}{3} \right) + \frac{1}{2} \right]; \quad f_n^{(3)} = \frac{e^{-iq_y}}{4} \left[\cos \left(\sqrt{3}q_x + \frac{2\pi(n-1)}{3} \right) + \frac{e^{3iq_y}}{2} \right]; \\ f_1^{(2)} &= \frac{1}{4} \left(2 \cos \frac{\sqrt{3}q_x}{2} \cos \frac{3q_y}{2} + \cos \sqrt{3}q_x \right); \quad f_2^{(2)} = \frac{1}{4} \left(\cos \sqrt{3}q_x - \cos \frac{\sqrt{3}q_x}{2} \cos \frac{3q_y}{2} - i\sqrt{3} \sin \frac{\sqrt{3}q_x}{2} \sin \frac{3q_y}{2} \right). \end{aligned} \quad (3)$$

Here $a_{i=1,2}^{(+)}$ and $b_{i=1,2}^{(+)}$ are projection operators onto $A_{1,2}$ and $B_{1,2}$ components of the 4-spinor in Eq. 1; $t_{i,j}^{(\lambda)}$ and $s_{i,j}^{(\lambda)}$ are the hopping and overlap parameters coupling i and j orbitals: neighbour rank λ identifies the coordination circle for the sites involved in a hop ($\lambda = 1$ corresponds to nearest-neighbour hop between different sublattice sites denoted as AB1 in Fig. 2a, $\lambda = 2$ is the shortest intra-sublattice hop denoted as AA1, $\lambda = 3$ is the second-neighbour inter-sublattice hop AB2, etc). The first term in \mathcal{H} describes on-site splitting of the orbitals due to SOC and account for six shortest ($\lambda = 2$) intra-

sublattice (A-A and B-B) hops. The second term describes three A-B and B-A hops, taking into account both closest ($\lambda = 1$) and next-neighbour ($\lambda = 3$) processes. An advantage of the proposed basis (1) is that each of the hopping elements is factorized into k-dependent functions $f_n^{(\lambda)}(\mathbf{q})$ and fitting parameters $P_n^{(\lambda)}$. The latter can be formally related to Slater-Koster (SK) parameters [48] for d- and p- orbitals $V_\alpha^{(s,\lambda)}$ of two types indicated by index $s = 0, 1$. Those marked by $s = 0$ correspond to two-centre SK integrals of spin-independent time-reversal-symmetric part of the one-electron Hamiltonian of the crystal; parameters with $s = 1$ are related

	$P_{1+}^{(\lambda)}$ (meV)	$P_{1-}^{(\lambda)}$ (meV)	$P_2^{(\lambda)}$ (meV)	$S_1^{(\lambda)}$	$S_2^{(\lambda)}$
$\lambda = 1$	122	31	-43	-2.88	0.91
$\lambda = 2$	-54	-151	-35	0.53	0.34
$\lambda = 3$	213	181	-243	-0.13	-0.20
On-site SOC ε_s			38 meV		

TABLE I. The values used for the parametrisation of the tight-binding model. The rows are for neighbour rank λ . The precision to which each value is given is based on sensitivity of the discrepancy between the TB and DFT spectra with respect to variation of the corresponding parameter.

to the time-reversal symmetry breaking by ferromagnetic ordering brought up by SOC. Similarly, the elements of the overlap matrix \mathcal{S} are expressed through two-center SK integrals but without any SOC contribution. Further details on hopping parameters are given in Supplemental Material [49], including a discussion of longer hops ($\lambda = 4, 5$).

The fitted values of TB parameters are listed in Table I and graphically represented in Fig. 2b. Figure 2c displays a direct comparison between the lowest spin-polarised conduction bands quadruplets computed using DFT (solid lines) and our TB model (dashed lines). A remarkable feature of the identified parameters is the relevance of hops beyond nearest-neighbour, in particular, the large magnitude of overlap parameters $S_{1,2}^{(1)}$. On the one hand a large inter-site overlap and the non-orthogonality of the basis (1) would make it difficult to use the proposed TB for many-body calculations. On the other hand, it points to that the hops are mediated by the halogens, which could be used to formulate a TB model with a basis expanded by, e.g., p -orbitals of halogens. This extension of the TB model we leave for future studies and, here, simply use the accurate semi-analytical description of the lowest conduction band in the quadruplet to analyse the charge transfer in CrX_3/G heterostructures.

III. GRAPHENE/ CrI_3 HETEROSTRUCTURE

In Fig. 2c, the lowest among the conduction band quadruplet of CrI_3 is quite flat. The details of the dispersion of this lowest band are elaborated using the semi-analytical description enabled by TB Hamiltonian (3) and are shown in Fig 3a. This band features six edge points Q, located approximately halfway along a $\Gamma - K$ path: here we identify three Q and Q' pairs related by time inversion of reciprocal space. The dispersion at the band minima is parabolic with slightly anisotropic effective masses $m_1 = 0.54m_0$, $m_2 = 0.58m_0$, m_0 being the free electron mass. An additional minimum at Γ point is located ≈ 3 meV above the band edge with an isotropic effective mass exceeding $10m_0$ producing a sufficiently high capacity of electron states for pinning the Fermi level

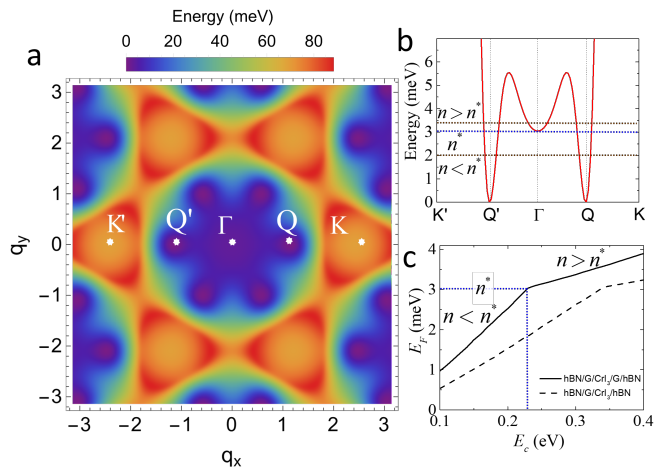


FIG. 3. Lower conduction band filling of CrI_3 monolayer. (a) The energy profile map of the lower conduction band; the band edge is at six Q, Q' points. (b) Lower energy band profile along $K' - \Gamma - K$ path. Below critical value of the doping n^* only the Q-point minima are filled, at the doping $n > n^*$ the filling of the minima at Γ begins. (c) The Fermi level relative to the band edge as a function of G- CrI_3 band offset for hBN/G/ CrI_3 /G/hBN (solid line) and hBN/G/ CrI_3 /hBN (dashed line) stacks. The regions corresponding to below critical and above critical value n^* are indicated.

in CrI_3 at high doping densities $n > n^*$. From this we conclude that in terms of doping the essential bandwidth of CrI_3 monolayer is ≈ 3 meV, so that the charge transfer into it from the environment such as graphene (Fig. 1) is determined by the interplay between the single-particle band offset, E_c , between the above-mentioned CrI_3 band and graphene Dirac point, electrostatics (classical capacitance), and Fermi level of holes in graphene (quantum capacitance contribution). The band edge profile along $K' - \Gamma - K$ direction is shown in Fig 3c.

It has been reported based on first-principles calculations that the electron affinity of the CrI_3 monolayer exceeds the work function of undoped graphene by $E_c \approx 0.2 - 0.4$ eV, suggesting a charge transfer between the layers in G/ CrI_3 heterostructures [3, 40]. A charge transfer of up to $\sim 10^{13} \text{ cm}^{-2}$, also electrically tunable has been observed experimentally for graphene- CrX_3 interfaces, X=I, Cl, Br [1, 2, 50–52]. While one reason for such transfer could be related to defects in the crystal, suggestion have been made that the observed graphene p-doping is associated with electron transfer into CrX_3 conduction band. Using the structure of the lowest conduction band of CrI_3 obtained by our modelling, we calculate the charge transfer for G/ CrI_3 /G and G/ CrI_3 stacks shown schematically in Fig. 4.

For G/ CrI_3 stack, the corresponding capacitor model is sketched in Fig. 4 (left). Here a difference V between the on-layer potential energies of graphene and CrI_3 layers

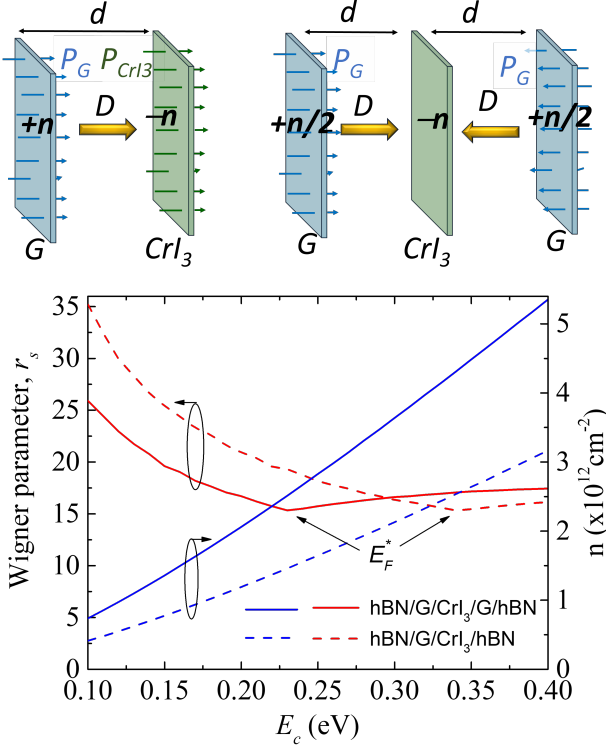


FIG. 4. **Charge transfer in CrI₃-graphene stacks.** Top: sketches illustrating charge transfer in a CrI₃/G stack (left) and G/CrI₃/G (right). The transferred sheet density n creates a positive charge at graphene and negative charge at CrI₃, producing a displacement field D and intra-layer polarisations (see Eqs. 4,5). Bottom: transferred carrier density, n (r.h.s. axis) and Wigner parameter, r_s (l.h.s. axis) as functions of the band offset, E_c . Solid lines correspond to hBN-encapsulated trilayer hBN/G/CrI₃/G/hBN, dashed lines correspond to hBN/G/CrI₃/hBN. E_F^* corresponds to Fermi level reaching the Γ point band edge.

can be expressed as

$$V = \frac{ed}{\epsilon_0} \left(en - \frac{P_G}{2} - \frac{P_{CrI_3}}{2} \right); P = (\epsilon - 1) \left(\frac{en}{2} - P \right), \quad (4)$$

where n is the sheet density of transferred carriers, d is the distance between the middle of the layers (i.e. carbon and chromium planes), ϵ_{G,CrI_3} are the out-of-plane dielectric susceptibilities of graphene and CrI₃ monolayers, n is the mobile charge sheet densities in the monolayers, P_{G,CrI_3} denote polarisations of the corresponding layers (see Fig. 4a). In the expression for V (Eq. 4) the first term in brackets is due to displacement field produced by the transferred charge in the layers; while two other terms take into account the layer's dielectric polarisations, as sketched in Fig. 4. Here we note that the out-of-plane polarisation of each layer is caused by the other layer, which is reflected by a factor of 1/2 in the expression for P in (Eq. 4) (because the dielectric polarisation of a monolayer is not affected by displacement

field generated by transferred charge of itself due to mirror reflection symmetry in each monolayer plane [53]).

For the case of CrI₃ sandwiched between two graphene layers, the corresponding capacitor model is sketched in Fig. 4 (right). In this case, the CrI₃ layer in the middle is not polarised, due to the symmetry of the structure. The expression for the electrostatic energy difference between a graphene and CrI₃ monolayer takes the form:

$$V = \frac{ed}{\epsilon_0} \left(en - \frac{P_G}{2} \right); P_G = (\epsilon_G - 1) \left(\frac{en}{2} - P_G \right), \quad (5)$$

where n is determined as electron density in CrI₃ (therefore, both graphene layers are doped with $n/2$ holes).

The carrier density in CrI₃, n , and the position of the Fermi level for both one- and two-graphene cases can be obtained from the overall charge neutrality of a stack, combined with Eqs. 4,5:

$$n = \frac{\epsilon_0 \alpha V}{e^2 d} = N_G \int_0^{E_c - V - E_F} \frac{2E dE}{\pi v^2 \hbar^2} = \int_0^{E_F} \rho(E) dE, \quad (6)$$

$$\alpha_{G/CrI_3} = \frac{4\epsilon_G \epsilon_{CrI_3}}{2\epsilon_G \epsilon_{CrI_3} + \epsilon_{CrI_3} + \epsilon_G}; \alpha_{G/CrI_3/G} = \frac{8\epsilon_G}{3\epsilon_G + 1},$$

where ρ is the density of states of the CrI₃ monolayer, and $N_G = 1, 2$ indicates the number of graphene layers in the stack. For numerical simulations we use $\epsilon_G = 2.6$ [53], $\epsilon_{CrI_3} = 4$ [21], and $d = 0.5$ nm [54]. The resulting dependence of E_F and n on the G/CrI₃ band offset, E_c , is shown in Figs. 3c and 4, respectively. The analysed interval of E_c covers the values suggested in Ref. [40]. We note that density n^* corresponds to $E_F^* \approx 0.2$ eV.

To assess how heavy are the electrons populating the CrI₃ band, we compute the Wigner parameter for the analysed interval of doping, Fig. 4. Unlike electrostatics determining the charge transfer discussed above, the Coulomb interaction within the layer largely depends on the in-plane polarisation properties of the media and encapsulation of the stacks, in particular hBN-encapsulated structures. For a bulk hexagonal BN encapsulation $\epsilon_{hBN} = \sqrt{\epsilon_{hBN}^{\parallel c} \epsilon_{hBN}^{\perp c}}$, where we take $\epsilon_{hBN}^{\parallel c} = 3.5$, $\epsilon_{hBN}^{\perp c} = 6.9$ for the dielectric constant parallel and perpendicular to c axes, respectively [55–57], resulting in $\epsilon_{hBN} = 4.9$. Then, we note that, due to spin+valley degeneracy, number of graphene layers (top and bottom), and steep dispersion of Dirac holes, screening of Coulomb repulsion of heavy electrons in magnetic layer by graphene is inefficient (in particular, because the average distance between the electrons in CrI₃ is much smaller than the Fermi wavelength of holes in graphene). Therefore, we determine the Wigner parameter as

$$r_s = \frac{e^2 \sqrt{n}}{4\pi \epsilon_{hBN} \epsilon_0 E_F},$$

and plot its computed values in Fig. 4. For the range of G/CrX₃ band offsets suggested in the recent literature

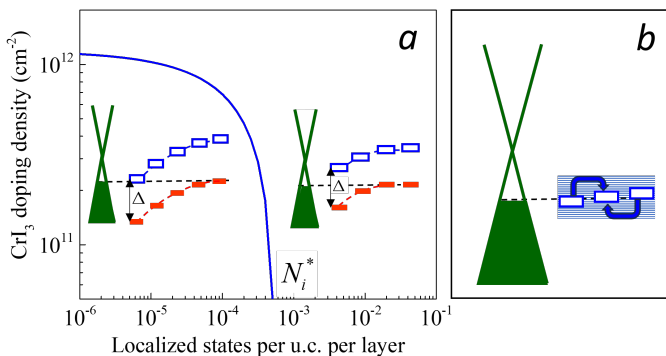


FIG. 5. **Sketch of a charge transfer between graphene and bulk CrI₃.** (a) In-gap defects ($\Delta \sim 0.5$ eV) in multiple CrI₃ layers reduce conduction band filling, completely quenching it when the number of localized states per unit cell in each monolayer is $N_i > N_i^*$, as computed for $E_c = 0.2$ eV. (b) CrI₃ conduction band broadening by the interlayer hybridization could also shrink the bandgap for a bulk material, hence, increasing a charge transfer from graphene.

the resulting r_s values fall in the range $15 < r_s < 20$, which indicate that heavy electrons in CrI₃ would be strongly correlated. As a result, here, we get a type-II semiconductor system hosting light highly-mobile holes in graphene(s) compensating heavy electrons in CrI₃, with a Wigner parameter almost in the range of Wigner crystallisation conditions.

IV. DISCUSSION

Based on the data presented in Fig. 4 we note that the charge transfer to CrI₃ monolayer band and the corresponding p-doping of graphene appears to be several times lower than the charger transfer evidenced by $\sim (5 - 10) \cdot 10^{12}$ cm⁻² graphene doping (both monolayer and bilayer) experimentally observed in one-sided-graphene on thick CrI₃ heterostructures [1, 2]. This discrepancy can be attributed to either a contribution of defects producing in-gap states [58], or to a substantial broadening of the conduction band in multi-layer CrI₃ by the interlayer hybridisation (thus shrinking the bandgap,

similar to what has been found in InSe [59, 60]).

We illustrate the influence of in-gap states in Fig. 5a by analysing a simultaneous filling of in-gap and band states for G/CrI₃ offset $E_c = 0.2$ eV and note that $N_i^* \sim 0.5 \cdot 10^{-3}$ defects per CrI₃ unit cell per layer would quench the conduction band occupancy by electron transfer into several CrI₃ layers near its surface. From this point of view, the suggested heterostructures based on monolayer CrI₃ would reduce the role of in-gap defects. Moreover, graphene-encapsulated CrI₃ monolayer (G/CrI₃/G) would be an even more promising system for bringing up the above-discussed strongly correlated heavy electrons.

As to the alternative option, related to the interlayer hybridization of CrI₃ band states, its careful quantitative description would require an extension of TB model (3) onto multi-layer structures. For developing such an extension it is worth noting a dominant role of the next-unit-cell hops between chromium orbital highlighted in Fig. 2b. The latter feature of the developed TB model can be attributed to involving of halogen orbitals as intermediate states in the hopping process. At the same time halogen orbitals should be accounted for in the interlayer hybridisation as the halogen ions are located in the outer sub-layers of the 2D crystal. This suggests an alternative formulation of a TB model for CrX₃ where the minimum number of Cr orbitals coupled by several neighbour hops will be superseded by a combination of Cr and halogen orbitals with only Cr-halogen and nearest-neighbour halogen-halogen hops (both within and between the layers).

V. ACKNOWLEDGEMENTS

We thank A. Geim, R. Gorbachev, A. Morpurgo, A. Principi, M. Yankowitz for stimulating discussions. We acknowledge support from EU Graphene Flagship Project, EPSRC Grants No. EP/S019367/1, No. EP/P026850/1, and No. EP/N010345/1, and EPSRC CDT Graphene-NOWNANO EP/L01548X/1, I.R. gratefully acknowledges the support of British Academy CARA Fellowship.

-
- [1] G. Tenasini, D. Soler-Delgado, Z. Wang, F. Yao, D. Dumcenco, E. Giannini, K. Watanabe, T. Taniguchi, C. Moultsdale, A. Garcia-Ruiz, V. I. Fal'ko, I. Gutiérrez-Lezama, and A. F. Morpurgo, Band gap opening in bilayer graphene-CrCl₃/CrBr₃/CrI₃ van der waals interfaces, *Nano Letters* **22**, 6760 (2022), pMID: 35930625, <https://doi.org/10.1021/acs.nanolett.2c02369>.
- [2] C.-C. Tseng, T. Song, Q. Jiang, Z. Lin, C. Wang, J. Suh, K. Watanabe, T. Taniguchi, M. A. McGuire, D. Xiao, J.-H. Chu, D. H. Cobden, X. Xu, and M. Yankowitz, Gate-tunable proximity effects in graphene on layered mag-

- netic insulators, *Nano Letters* **22**, 8495 (2022), pMID: 36279401, <https://doi.org/10.1021/acs.nanolett.2c02931>.
- [3] C. Cardoso, A. T. Costa, A. H. MacDonald, and J. Fernández-Rossier, Strong magnetic proximity effect in van der waals heterostructures driven by direct hybridization, *Phys. Rev. B* **108**, 184423 (2023).
- [4] H. Kurebayashi, J. H. Garcia, S. Khan, J. Sinova, and S. Roche, Magnetism, symmetry and spin transport in van der waals layered systems, *Nature Reviews Physics* **4**, 150 (2022).

- [5] B. Huang, M. A. McGuire, A. F. May, D. Xiao, P. Jarillo-Herrero, and X. Xu, Emergent phenomena and proximity effects in two-dimensional magnets and heterostructures, *Nature Materials* **19**, 1276 (2020).
- [6] D. Soriano, M. I. Katsnelson, and J. Fernández-Rossier, Magnetic two-dimensional chromium trihalides: A theoretical perspective, *Nano Letters* **20**, 6225 (2020).
- [7] K. S. Burch, D. Mandrus, and J.-G. Park, Magnetism in two-dimensional van der waals materials, *Nature* **563**, 47 (2018).
- [8] Q. H. Wang, A. Bedoya-Pinto, M. Blei, A. H. Dismukes, A. Hamo, S. Jenkins, M. Koperski, Y. Liu, Q.-C. Sun, E. J. Telford, H. H. Kim, M. Augustin, U. Vool, J.-X. Yin, L. H. Li, A. Falin, C. R. Dean, F. Casanova, R. F. L. Evans, M. Chshiev, A. Mishchenko, C. Petrovic, R. He, L. Zhao, A. W. Tseng, B. D. Gerardot, M. Brotons-Gisbert, Z. Guguchia, X. Roy, S. Tongay, Z. Wang, M. Z. Hasan, J. Wrachtrup, A. Yacoby, A. Fert, S. Parkin, K. S. Novoselov, P. Dai, L. Balicas, and E. J. G. Santos, The magnetic genome of two-dimensional van der waals materials, *ACS Nano* **16**, 6960 (2022).
- [9] M. Gibertini, M. Koperski, A. F. Morpurgo, and K. S. Novoselov, Magnetic 2d materials and heterostructures, *Nature Nanotechnology* **14**, 408 (2019).
- [10] M. A. McGuire, H. Dixit, V. R. Cooper, and B. C. Sales, Coupling of crystal structure and magnetism in the layered, ferromagnetic insulator CrI₃, *Chemistry of Materials* **27**, 612 (2015).
- [11] M.-C. Wang, C.-C. Huang, C.-H. Cheung, C.-Y. Chen, S. G. Tan, T.-W. Huang, Y. Zhao, Y. Zhao, G. Wu, Y.-P. Feng, H.-C. Wu, and C.-R. Chang, Prospects and opportunities of 2d van der waals magnetic systems, *Annalen der Physik* **532**, 1900452 (2020), <https://onlinelibrary.wiley.com/doi/pdf/10.1002/andp.201900452>.
- [12] L. Thiel, Z. Wang, M. A. Tschudin, D. Rohner, I. Gutiérrez-Lezama, N. Ubrig, M. Gibertini, E. Giannini, A. F. Morpurgo, and P. Maletinsky, Probing magnetism in 2d materials at the nanoscale with single-spin microscopy, *Science* **364**, 973 (2019), <https://www.science.org/doi/pdf/10.1126/science.aav6926>.
- [13] F. Yao, V. Multian, Z. Wang, N. Ubrig, J. Teyssier, F. Wu, E. Giannini, M. Gibertini, I. Gutiérrez-Lezama, and A. F. Morpurgo, Multiple antiferromagnetic phases and magnetic anisotropy in exfoliated CrBr₃ multilayers, *Nature Communications* **14**, 4969 (2023).
- [14] Q. Yang, X. Hu, X. Shen, A. V. Krasheninnikov, Z. Chen, and L. Sun, Enhancing ferromagnetism and tuning electronic properties of CrI₃ monolayers by adsorption of transition-metal atoms, *ACS Applied Materials & Interfaces* **13**, 21593 (2021).
- [15] X. Lu, R. Fei, and L. Yang, Curie temperature of emerging two-dimensional magnetic structures, *Phys. Rev. B* **100**, 205409 (2019).
- [16] H. Zhu, Y. Gao, Y. Hou, Z. Gui, and L. Huang, Tunable magnetic anisotropy in two-dimensional CrX₃/AlN ($x = \text{I, Br, Cl}$) heterostructures, *Phys. Rev. B* **106**, 134412 (2022).
- [17] D. Staros, G. Hu, J. Tiihonen, R. Nanguneri, J. Krogel, M. C. Bennett, O. Heinonen, P. Ganesh, and B. Rubenstein, A combined first principles study of the structural, magnetic, and phonon properties of monolayer CrI₃, *The Journal of Chemical Physics* **156**, 014707 (2022), https://pubs.aip.org/aip/jcp/article-pdf/doi/10.1063/5.0074848/16535185/014707_1.online.pdf.
- [18] S. Acharya, D. Pashov, B. Cunningham, A. N. Rudenko, M. Rösner, M. Grüning, M. van Schilfgaarde, and M. I. Katsnelson, Electronic structure of chromium trihalides beyond density functional theory, *Phys. Rev. B* **104**, 155109 (2021).
- [19] Y. O. Kvashnin, A. Bergman, A. I. Lichtenstein, and M. I. Katsnelson, Relativistic exchange interactions in CrX₃ ($x = \text{Cl, Br, I}$) monolayers, *Phys. Rev. B* **102**, 115162 (2020).
- [20] M. Wu, Z. Li, and S. G. Louie, Optical and magneto-optical properties of ferromagnetic monolayer CrBr₃: A first-principles gw and gw plus bethe-salpeter equation study, *Phys. Rev. Mater.* **6**, 014008 (2022).
- [21] M. Wu, Z. Li, T. Cao, and S. G. Louie, Physical origin of giant excitonic and magneto-optical responses in two-dimensional ferromagnetic insulators, *Nature Communications* **10**, 2371 (2019).
- [22] M. Akram, H. LaBollita, D. Dey, J. Kapeghian, O. Erten, and A. S. Botana, Moiré skyrmions and chiral magnetic phases in twisted CrX₃ ($X = \text{I, Br, and Cl}$) bilayers, *Nano Letters* **21**, 6633 (2021).
- [23] R. A. Beck, L. Lu, P. V. Sushko, X. Xu, and X. Li, Defect-induced magnetic skyrmion in a two-dimensional chromium triiodide monolayer, *JACS Au* **1**, 1362 (2021).
- [24] A. O. Fumega and J. L. Lado, Moiré-driven multiferroic order in twisted CrCl₃, CrBr₃ and CrI₃ bilayers, *2D Materials* **10**, 025026 (2023).
- [25] H. Xie, X. Luo, G. Ye, Z. Ye, H. Ge, S. H. Sung, E. Rennich, S. Yan, Y. Fu, S. Tian, H. Lei, R. Hovden, K. Sun, R. He, and L. Zhao, Twist engineering of the two-dimensional magnetism in double bilayer chromium triiodide homostructures, *Nature Physics* **18**, 30 (2022).
- [26] K. Dolui, M. D. Petrović, K. Zollner, P. Plecháč, J. Fabian, and B. K. Nikolić, Proximity spin-orbit torque on a two-dimensional magnet within van der waals heterostructure: Current-driven antiferromagnet-to-ferromagnet reversible nonequilibrium phase transition in bilayer CrI₃, *Nano Letters* **20**, 2288 (2020).
- [27] K. W. Song and V. I. Fal'ko, Superexchange and spin-orbit coupling in monolayer and bilayer chromium trihalides, *Phys. Rev. B* **106**, 245111 (2022).
- [28] K. W. Song, Interlayer superexchange in bilayer chromium trihalides, *Phys. Rev. B* **107**, 245133 (2023).
- [29] D. Soriano, C. Cardoso, and J. Fernández-Rossier, Interplay between interlayer exchange and stacking in CrI₃ bilayers, *Solid State Communications* **299**, 113662 (2019).
- [30] R. A. Beck, S. Sun, X. Xu, D. R. Gamelin, T. Cao, and X. Li, Understanding external pressure effects and interlayer orbital exchange pathways in the two-dimensional magnet-chromium triiodide, *The Journal of Physical Chemistry C* **126**, 19327 (2022).
- [31] A. Ghosh, D. Singh, T. Aramaki, Q. Mu, V. Borisov, Y. Kvashnin, G. Haider, M. Jonak, D. Chareev, S. A. Medvedev, R. Klingeler, M. Mito, E. H. Abdul-Hafidh, J. Vejpravova, M. Kalbáč, R. Ahuja, O. Eriksson, and M. Abde-Hafiez, Exotic magnetic and electronic properties of layered CrI₃ single crystals under high pressure, *Phys. Rev. B* **105**, L081104 (2022).
- [32] D. R. Klein, D. MacNeill, Q. Song, D. T. Larson, S. Fang, M. Xu, R. A. Ribeiro, P. C. Canfield, E. Kaxiras, R. Comin, and P. Jarillo-Herrero, Enhancement of interlayer exchange in an ultrathin two-dimensional magnet, *Nature Physics* **15**, 1255 (2019).

- [33] L. Webster and J.-A. Yan, Strain-tunable magnetic anisotropy in monolayer crcl_3 , crbr_3 , and cri_3 , *Phys. Rev. B* **98**, 144411 (2018).
- [34] D. Zhong, K. L. Seyler, X. Linpeng, N. P. Wilson, T. Taniguchi, K. Watanabe, M. A. McGuire, K.-M. C. Fu, D. Xiao, W. Yao, and X. Xu, Layer-resolved magnetic proximity effect in van der waals heterostructures, *Nature Nanotechnology* **15**, 187 (2020).
- [35] Y. Wu, Q. Cui, M. Zhu, X. Liu, Y. Wang, J. Zhang, X. Zheng, J. Shen, P. Cui, H. Yang, and S. Wang, Magnetic exchange field modulation of quantum hall ferromagnetism in 2d van der waals crcl_3 /graphene heterostructures, *ACS Applied Materials & Interfaces* **13**, 10656 (2021).
- [36] Z. Wu, J. Yu, and S. Yuan, Strain-tunable magnetic and electronic properties of monolayer cri_3 , *Physical Chemistry Chemical Physics* **21**, 7750 (2019).
- [37] A. B. Georgescu, A. J. Millis, and J. M. Rondinelli, Trigonal symmetry breaking and its electronic effects in the two-dimensional dihalides mX_2 and trihalides mX_3 , *Phys. Rev. B* **105**, 245153 (2022).
- [38] M. Grzeszczyk, S. Acharya, D. Pashov, Z. Chen, K. Vaklinova, M. van Schilfgaarde, K. Watanabe, T. Taniguchi, K. S. Novoselov, M. I. Katsnelson, and M. Koperski, Strongly correlated exciton-magnetization system for optical spin pumping in crbr_3 and cri_3 , *Advanced Materials* **35**, 2209513 (2023), <https://onlinelibrary.wiley.com/doi/pdf/10.1002/adma.202209513>
- [39] Z. Wu, J. Yu, and S. Yuan, Strain-tunable magnetic and electronic properties of monolayer cri_3 , *Phys. Chem. Chem. Phys.* **21**, 7750 (2019).
- [40] J. Zhang, B. Zhao, T. Zhou, Y. Xue, C. Ma, and Z. Yang, Strong magnetization and chern insulators in compressed graphene/ cri_3 van der waals heterostructures, *Phys. Rev. B* **97**, 085401 (2018).
- [41] N. Ubrig, Z. Wang, J. Teyssier, T. Taniguchi, K. Watanabe, E. Giannini, A. F. Morpurgo, and M. Gibertini, Low-temperature monoclinic layer stacking in atomically thin cri_3 crystals, *2D Materials* **7**, 015007 (2019).
- [42] Z. Liu, Y. Guo, Z. Chen, T. Gong, Y. Li, Y. Niu, Y. Cheng, H. Lu, L. Deng, and B. Peng, Observation of intrinsic crystal phase in bare few-layer cri_3 , *Nanophotonics* **11**, 4409 (2022).
- [43] T. Li, S. Jiang, N. Sivadas, Z. Wang, Y. Xu, D. Weber, J. E. Goldberger, K. Watanabe, T. Taniguchi, C. J. Fennie, K. Fai Mak, and J. Shan, Pressure-controlled interlayer magnetism in atomically thin CrI_3 , *Nature Materials* **18**, 1303 (2019).
- [44] S. Djurdji \acute{e} Mijin, A. Šolajić, J. Pešić, M. Šćepanović, Y. Liu, A. Baum, C. Petrovic, N. Lazarević, and Z. V. Popović, Lattice dynamics and phase transition in cri_3 single crystals, *Phys. Rev. B* **98**, 104307 (2018).
- [45] P. Giannozzi, S. Baroni, N. Bonini, M. Calandra, R. Car, C. Cavazzoni, D. Ceresoli, G. L. Chiarotti, M. Cococcioni, I. Dabo, A. D. Corso, S. de Gironcoli, S. Fabris, G. Fratesi, R. Gebauer, U. Gerstmann, C. Gougoussis, A. Kokalj, M. Lazzeri, L. Martin-Samos, N. Marzari, F. Mauri, R. Mazzarello, S. Paolini, A. Pasquarello, L. Paulatto, C. Sbraccia, S. Scandolo, G. Sclauzero, A. P. Seitsonen, A. Smogunov, P. Umari, and R. M. Wentzcovitch, Quantum espresso: a modular and open-source software project for quantum simulations of materials, *Journal of Physics: Condensed Matter* **21**, 395502 (2009).
- [46] P. Giannozzi, O. Andreussi, T. Brumme, O. Bunau, M. B. Nardelli, M. Calandra, R. Car, C. Cavazzoni, D. Ceresoli, M. Cococcioni, N. Colonna, I. Carnimeo, A. D. Corso, S. de Gironcoli, P. Delugas, R. A. DiStasio, A. Ferretti, A. Floris, G. Fratesi, G. Fugallo, R. Gebauer, U. Gerstmann, F. Giustino, T. Gorni, J. Jia, M. Kawamura, H.-Y. Ko, A. Kokalj, E. Küçükbenli, M. Lazzeri, M. Marsili, N. Marzari, F. Mauri, N. L. Nguyen, H.-V. Nguyen, A. O. de-la Roza, L. Paulatto, S. Ponc \acute{e} , D. Rocca, R. Sabatini, B. Santra, M. Schlipf, A. P. Seitsonen, A. Smogunov, I. Timrov, T. Thonhauser, P. Umari, N. Vast, X. Wu, and S. Baroni, Advanced capabilities for materials modelling with quantum espresso, *Journal of Physics: Condensed Matter* **29**, 465901 (2017).
- [47] J. P. Perdew, K. Burke, and M. Ernzerhof, Generalized gradient approximation made simple, *Phys. Rev. Lett.* **77**, 3865 (1996).
- [48] J. C. Slater and G. F. Koster, Simplified lcao method for the periodic potential problem, *Phys. Rev.* **94**, 1498 (1954).
- [49] [URL_will_be_inserted_by_publisher.](#)
- [50] Y. Zhang, J. Liu, R. Deng, X. Shi, H. Tang, H. Chen, and H. Yuan, Electronic structure, magnetoresistance and spin filtering in graphene—2 monolayer- CrI_3 —graphene van der waals magnetic tunnel junctions, *RSC Adv.* **12**, 28533 (2022).
- [51] S. Jiang, L. Li, Z. Wang, K. F. Mak, and J. Shan, Controlling magnetism in 2d cri_3 by electrostatic doping, *Nature Nanotechnology* **13**, 549 (2018).
- [52] S. Jiang, L. Li, Z. Wang, J. Shan, and K. F. Mak, Spin tunnel field-effect transistors based on two-dimensional van der waals heterostructures, *Nature Electronics* **2**, 159 (2019).
- [53] S. Slizovskiy, A. Garcia-Ruiz, A. I. Berdyugin, N. Xin, T. Taniguchi, K. Watanabe, A. K. Geim, N. D. Drummond, and V. I. Fal’ko, Out-of-plane dielectric susceptibility of graphene in twistrionic and bernal bilayers, *Nano Letters* **21**, 6678 (2021), pMID: 34296602, <https://doi.org/10.1021/acs.nanolett.1c02211>.
- [54] M. U. Farooq and J. Hong, Switchable valley splitting by external electric field effect in graphene/ cri_3 heterostructures, *npj 2D Materials and Applications* **3**, 3 (2019).
- [55] A. Laturia, M. L. Van de Put, and W. G. Vandenberghe, Dielectric properties of hexagonal boron nitride and transition metal dichalcogenides: from monolayer to bulk, *npj 2D Materials and Applications* **2**, 6 (2018).
- [56] A. Pierret, D. Mele, H. Graef, J. Palomo, T. Taniguchi, K. Watanabe, Y. Li, B. Toury, C. Journet, P. Steyer, V. Garnier, A. Loiseau, J.-M. Berroir, E. Bocquillon, G. Fève, C. Voisin, E. Baudin, M. Rosticher, and B. Plaçais, Dielectric permittivity, conductivity and breakdown field of hexagonal boron nitride, *Materials Research Express* **9**, 065901 (2022).
- [57] N. Ohba, K. Miwa, N. Nagasako, and A. Fukumoto, First-principles study on structural, dielectric, and dynamical properties for three bn polytypes, *Phys. Rev. B* **63**, 115207 (2001).
- [58] J. Zhang, Y. Guo, P. Li, J. Wang, S. Zhou, J. Zhao, D. Guo, and D. Zhong, Imaging vacancy defects in single-layer chromium triiodide, *The Journal of Physical Chemistry Letters* **12**, 2199 (2021), pMID: 33630596, <https://doi.org/10.1021/acs.jpcllett.1c00112>.
- [59] S. J. Magorrian, V. Zólyomi, and V. I. Fal’ko, Electronic and optical properties of two-dimensional inorganic from a

- dft-parametrized tight-binding model, [Phys. Rev. B **94**, 245431 \(2016\)](#).
- [60] D. A. Bandurin, A. V. Tyurnina, G. L. Yu, A. Mishchenko, V. Zólyomi, S. V. Morozov, R. K. Kumar, R. V. Gorbachev, Z. R. Kudrynskiy, S. Pezzini, Z. D. Kovalyuk, U. Zeitler, K. S. Novoselov, A. Patané, L. Eaves, I. V. Grigorieva, V. I. Fal'ko, A. K. Geim, and Y. Cao, High electron mobility, quantum hall effect and anomalous optical response in atomically thin inSe, [Nature Nanotechnology **12**, 223 \(2017\)](#).